

AuPd Metal Nanoparticles as Probes of Nanoscale Thermal Transport in Aqueous Solution

Zhenbin Ge,* David G. Cahill, and Paul V. Braun

Department of Materials Science and Engineering, the Frederick Seitz Materials Research Laboratory, and the Beckman Institute for Advanced Science and Technology, University of Illinois, Urbana, Illinois 61801

Received: April 13, 2004; In Final Form: July 9, 2004

Water- and alcohol-soluble AuPd nanoparticles have been investigated to determine the effect of the organic stabilizing group on the thermal conductance G of the particle/fluid interface. The thermal decays of tiopronin-stabilized 3–5-nm diameter AuPd alloy nanoparticles, thioalkylated ethylene glycol-stabilized 3–5-nm diameter AuPd nanoparticles, and cetyltrimethylammonium bromide-stabilized 22-nm diameter Au-core/AuPd-shell nanoparticles give thermal conductances $G \approx 100\text{--}300 \text{ MW m}^{-2} \text{ K}^{-1}$ for the particle/water interfaces, approximately an order of magnitude larger than the conductance of the interfaces between alkanethiol-terminated AuPd nanoparticles and toluene. The similar values of G for particles ranging in size from 3 to 24 nm with widely varying surface chemistry indicate that the thermal coupling between AuPd nanoparticles and water is strong regardless of the self-assembled stabilizing group.

1. Introduction

Thermal transport on nanometer scales plays an important role in determining the performance of many state-of-the-art engineering systems.^{1–3} The promise of nanostructured materials for increasing the efficiency of thermoelectric energy conversion,^{3–5} for improving heat conduction in composites⁶ and heat transfer fluids,^{7,8} and for targeted thermal effects in medical therapies⁹ and photothermally activated drug delivery¹⁰ all depend critically on thermal transport across solid–solid or solid–fluid interfaces. Highly controlled surface chemistries of gold nanoparticles have been used as a probe of thermal transport across solid–fluid interfaces¹¹ because gold nanoparticles can be functionalized with a large number of organic ligands through thiol chemistries^{12,13} or charge stabilization,¹⁴ and gold nanoparticles are chemically stable and generally biocompatible.¹⁵ The decay of electronic and vibrational excited states of metal nanoparticles and the dependence of these decay rates on interface and solvent effects have been extensively studied by transient absorption.^{16–21} Thermal transport can also provide a novel probe of nanoparticle structure: Hartland and co-workers²² recently studied heat dissipation in gold–silica core–shell nanoparticles in both water and ethanol solutions and found that the characteristic time constant for heat dissipation depends on the microstructure of the silica shell.

The focus of our work is measurements of the thermal conductance G of the particle/fluid interface: G relates the temperature drop ΔT at an interface to the flux of heat F that crosses the interface, $F = G\Delta T$.^{2,11} We determine G by analyzing the decay of the nanoparticle temperature following heating by an ultrashort laser pulse. Quantitative analysis of the data requires a complete solution of the differential equations that describe the flow of heat from the particle through the particle/fluid interface and into the surrounding fluid. Those equations and their exact numerical solutions are described below.

A relatively simple argument, however, provides insight on what combinations of nanoparticle radius r and interface thermal conductance G are needed for G to play an important role in

the cooling of a rapidly heated nanoparticle. For sufficiently large nanoparticles or nanoparticles with interfaces of high thermal conductance, the decay of the nanoparticle temperature will be limited by the diffusion of heat in the surrounding fluid; the characteristic time τ_d for this process can be estimated by equating the heat capacity of the particle $\frac{4}{3}\pi r^3 C_p$ to the heat capacity of a layer of the surrounding fluid with the thickness of the thermal diffusion length, $4\pi r^2 C_f \sqrt{D_f \tau_d}$, and solving for τ_d

$$\tau_d = \frac{r^2 C_p^2}{9 C_f \Lambda_f} \quad (1)$$

where C_p and C_f are the heat capacities per unit volume of the particle and the fluid, and Λ_f is the thermal conductivity of the fluid. For sufficiently small nanoparticles or nanoparticles with interfaces of low interface thermal conductance, the cooling rate of the nanoparticle will be limited by G and the time-scale of the exponential decay of the particle temperature is given by the ratio of the heat capacity of the particle to the total thermal conductance of the particle–fluid interface,

$$\tau_i = \frac{r C_p}{3G} \quad (2)$$

Interface effects, i.e., the finite value of G , will become important when τ_i is comparable to τ_d . Setting $\tau_i = \tau_d$ defines a critical value of G that demarcates the regime of cooling controlled by interface thermal conductance from the regime of cooling that is controlled by the diffusion of heat in the surrounding fluid,

$$G_c = \frac{3 C_f \Lambda_f}{r C_p} \quad (3)$$

With $G \gg G_c$, the cooling rate is controlled by the effusivity of the fluid $\Lambda_f C_f$. With $G \ll G_c$, the cooling rate is controlled by the interface thermal conductance G . For example, with $r = 10 \text{ nm}$, C_p for Au, and C_f , Λ_f for water, $G_c = 300 \text{ MW m}^{-2} \text{ K}^{-1}$. In our prior work on citrate-stabilized Pt nanoparticles,

* Address correspondence to this author. E-mail: zge@uiuc.edu. Phone: 1-217-244-8107. Fax: 1-217-333-2736.

we found $G \approx 130 \text{ MW m}^{-2} \text{ K}^{-1}$ and, if this value for G is typical of interfaces with water, we can expect that interface effects will play an important role in the cooling of particles in water as long as $r < 20 \text{ nm}$.

In our initial study of the interface thermal conductance of solid–fluid interfaces, we employed colloidal dispersions of 3–10 nm diameter, alkanethiol-stabilized, Au and AuPd nanoparticles in toluene and 10 nm Pt nanoparticles in water.¹¹ A key result of this work was that the thermal conductance of Pt nanoparticle interfaces with water is surprisingly large, comparable to the thermal conductance of typical solid–solid interfaces² and an order of magnitude larger than the thermal conductance of interfaces between nanoparticles and organic solvents¹¹ or between nanotubes and surfactants.⁸ The focus of the present study is to address the generality of our observation of high interface thermal conductance in aqueous suspensions through experiments on three new combinations of organic stabilizing group and nanoparticle sizes. We use AuPd nanoparticles in these studies because they exhibit long-term stability and favorable optical properties, and are amenable to surface modification through Au-thiol chemistries.

2. Experimental Section

The tiopronin-protected AuPd alloy nanoparticles were synthesized by co-reduction of PdCl_2 and HAuCl_4 in single-phase reduction following a literature preparation.¹² Briefly, PdCl_2 was first dissolved in HCl and aged for a week before the synthesis. HAuCl_4 (0.36 mmol), PdCl_2 (0.09 mmol, 1.8 mL, 50 mM in HCl solution), and *N*-(2-mercaptopropionyl)glycine (tiopronin) (0.45 mmol) were co-dissolved in 10 mL of methanol, resulting in an orange brown solution. NaBH_4 (10 mmol) in 10 mL of H_2O was added with rapid stirring. The resulting black suspension was stirred for overnight. The solvent was then removed by using a rota-evaporator with mild heating. The crude tiopronin-stabilized AuPd nanoparticles were dissolved in water and then precipitated by adjusting the pH to 2. After centrifuging and removing the supernatant, the particles were redissolved in DI-water and then purified by dialysis. The pH of the final solution is ~ 6 , thus most of the tiopronin will be deprotonated resulting in additional charge repulsive interactions, stabilizing the particles.

Thioalkylated ethylene glycol-stabilized AuPd alloy nanoparticles were synthesized by co-reduction of PdCl_2 and HAuCl_4 in single-phase reduction following a literature preparation.¹³ HAuCl_4 (0.24 mmol), PdCl_2 (0.06 mmol, 1.2 mL, 50 mM in HCl solution), and monohydroxy(1-mercaptopundec-11-yl)tetraethylene glycol (EG4) (0.24 mmol) prepared as described by Pale-Grosdemange et al.²³ were co-dissolved in 150 mL of 2-propanol and 1.5 mL of acetic acid. Freshly prepared NaBH_4 (10 mmol) in 15 mL of methanol was added with rapid stirring. After further stirring for 8 h, the solution were concentrated and then precipitated in hexane. The supernatant was decanted and the solid product was washed with hexane 5 times.

Au core–AuPd shell nanoparticles were synthesized by modification of seeded growth methods.^{14,24} First, 13-nm citrate-stabilized Au seed particles were prepared²⁵ and used without modification. Second, 4 sets of 50-mL conical flasks were labeled A, B, C, and D. Each contained 10 mL of 1 mM K_2PdCl_4 , 10 mL of 1 mM HAuCl_4 aqueous solution, and 0.2 mmol of cetyltrimethylammonium bromide (CTAB). The mixtures were stirred with heating until the solution turned a clear orange color. Freshly prepared ascorbic acid aqueous solution (2 mL, 100 mM) was added to each growth solution A, B, C, and D. Next, 8, 10, 15, and 20 mL of the seed solution

were added to the growth solutions A, B, C, and D, respectively, and the reaction solutions were stirred for 4 h. The particles were purified by centrifuging and decanting the supernatant. The resulting products are denoted as AuPd-A, AuPd-B, AuPd-C, and AuPd-D.

For comparisons with water-soluble particles, 1-dodecanethiol (DodSH)-stabilized AuPd alloy nanoparticles were synthesized by co-reduction of PdCl_2 and HAuCl_4 in a Brust-type synthesis.²⁶ For $\text{Au}_{0.8}\text{Pd}_{0.2}$, 0.56 mmol of HAuCl_4 and 0.14 mmol of PdCl_2 (2.8 mL, 50 mM in HCl solution) were dissolved in 20 mL of DI-water. Phase transfer to toluene was carried out with TOABr (60 mL, 25 mM). DodSH (0.2 mmol) was first dissolved in 5 mL of toluene and added to the organic phase. Reduction took place following dropwise addition of NaBH_4 (20 mL, 0.4 M) and the mixture was stirred for 4 h. The organic phase was collected, concentrated, and precipitated twice from excess ethanol by centrifugation.

Transmission electron microscopy (TEM) images obtained with a Philips CM12 microscope were used to determine the particle sizes. Composition profiles of Au-core/AuPd-shell particles were characterized by scanning transmission electron microscopy (STEM) and energy-dispersive spectroscopy (EDS) on a VG HB501 STEM. TEM/STEM specimens were made by placing 10 μL of a water suspension of nanoparticles on a carbon-coated copper grid. Average compositions of the AuPd alloy particles were measured by X-ray fluorescence spectroscopy (XRF), using a KEVEX Analyst 770 spectrometer. A standard UV–vis spectrometer was used to characterize the optical absorption of the nanoparticle suspensions.

The transient absorption data were collected with a mode-locked Ti:sapphire laser that produces a series of $<0.5 \text{ ps}$ pulses at a repetition rate of 80.6 MHz. The laser output is split into a “pump” beam and a “probe” beam whose relative optical path lengths are adjusted via a mechanical delay stage. We modified our thermoreflectance apparatus¹ to accommodate transmission measurements.¹¹ A 20 mm focal length microscope objective focuses the pump and probe beams and also forms a reflected-light dark-field microscopy image of the sample cell on a CCD camera.²⁷ The fluid cells are $0.2 \times 2 \text{ mm}^2$ flat-sided capillary tubes epoxied to a steel disk that serves as a heat sink and sample holder. We use pump and probe beam powers of 5–15 mW, a wavelength of 770 nm, and a $1/e^2$ beam radius of 8 μm . The differences in transmitted probe intensity caused by the pump pulse appear at the $f = 9.8 \text{ MHz}$ modulation frequency of the pump beam and are extracted with lock-in detection.²⁷

Our measurement scheme differs from a majority of related studies in the literature by the fact that we use the fundamental output of the Ti:sapphire laser oscillator without amplification or frequency conversion. The high repetition rate and high signal-to-noise of our system—the noise level for measurements of changes in optical absorption is $10^{-7}/\sqrt{\text{Hz}}$ ²⁷—allows us to work with extremely small temperature excursions for the particles: the peak energy density of the pump pulses is $E \approx 0.2 \text{ mJ cm}^{-2}$. We estimate the average temperature rise of the AuPd particles by $\Delta T = \alpha E / (C_p V_f)$, where α is the optical absorption coefficient, V_f is the volume fraction of the nanoparticles in the suspension, and C_p is the heat capacity of the nanoparticles per unit volume; with $\alpha \approx 1 \text{ cm}^{-1}$ and $V_f \approx 4 \times 10^{-5}$, $\Delta T = 2 \text{ K}$. Therefore our experiments are always in the limit of small temperature excursions, $\Delta T/T \ll 1$, and we can safely assume that changes in optical absorption of the suspension are a linear function of ΔT .

Our use of the fundamental wavelength of the Ti:sapphire laser for both the pump and probe beams greatly simplifies the

experiment and essentially eliminates any problems with the photochemical stability of the nanoparticle suspensions. But this choice of pump and probe wavelength also introduces constraints on the materials systems that can be studied. For example, the transient absorption signals recorded for pure Au nanoparticles are weak and the thermal decays that we seek to analyze are easily masked at short delay times by electronic effects. In our previous work, we identified the addition of Pd to Au nanoparticles as a way of increasing the transient absorption signal; AuPd alloys have a significantly larger optical absorption at $\lambda \approx 770$ nm than pure Au and the changes in the optical absorption with temperature are also larger.

Since the thermal decay times of the nanoparticles are much longer than the width of the pump pulse and are much shorter than the oscillation period of the model-locked laser, the transient absorption measurements are relatively easily interpreted as a direct measurement of the temporal evolution of the temperature of the particle subjected to an instantaneous source of heat. An analysis of the particle temperature is, however, more easily accomplished by first solving the equations that describe the flow of heat by using a periodic heat source, i.e., by solving the equations in the frequency domain.

In spherical coordinates, the frequency-domain solution to the diffusion equation in the fluid is

$$T = \frac{rT_f}{\rho} \exp(-q(\rho - r)) \quad (4)$$

where T_f is the temperature of the fluid adjacent to the particle, ρ is the radial coordinate, r is the particle radius, and $1/q$ is the complex thermal wavelength, $q^2 = i\omega/D_f$, $D_f = \Lambda_f/C_f$.

The temperature of the particle T_p is determined by a balance between the heat needed to change the temperature of the particle, heating from the source term P , and cooling by the flux of heat F flowing through the interface between the particle and the fluid. (The temperature gradient within the particle is negligible.)

$$\frac{4\pi}{3}i\omega r^3 C_p T_p = P - 4\pi r^2 F \quad (5)$$

The radiative boundary condition for the temperature relates the heat flux to the temperature of the particle and the temperature of the fluid near the interface,

$$G(T_p - T_f) = F \quad (6)$$

Continuity of the heat flux in the fluid $F = -\Lambda_f dT/d\rho$ gives

$$rF = T_f(1 + qr)\Lambda_f \quad (7)$$

These three algebraic equations, eqs 5–7, are then solved for T_p by eliminating F and T_f . Thus, an analytical solution for T_p , while cumbersome, is relatively straightforward in the frequency domain. As discussed above, temperature excursions in our experiments are small and therefore changes in optical absorption of the probe beam will be a linear function of the particle temperature. The in-phase signal of the lock-in amplifier is then¹

$$S(q) = T_p(q/\tau + f) + T_p(q/\tau - f) \quad (8)$$

$$V_{in}(t) = A \sum_{q=-\infty}^{\infty} S(q) \exp(i2\pi tq/\tau) \quad (9)$$

where τ is the time between pulses, t is the time delay between

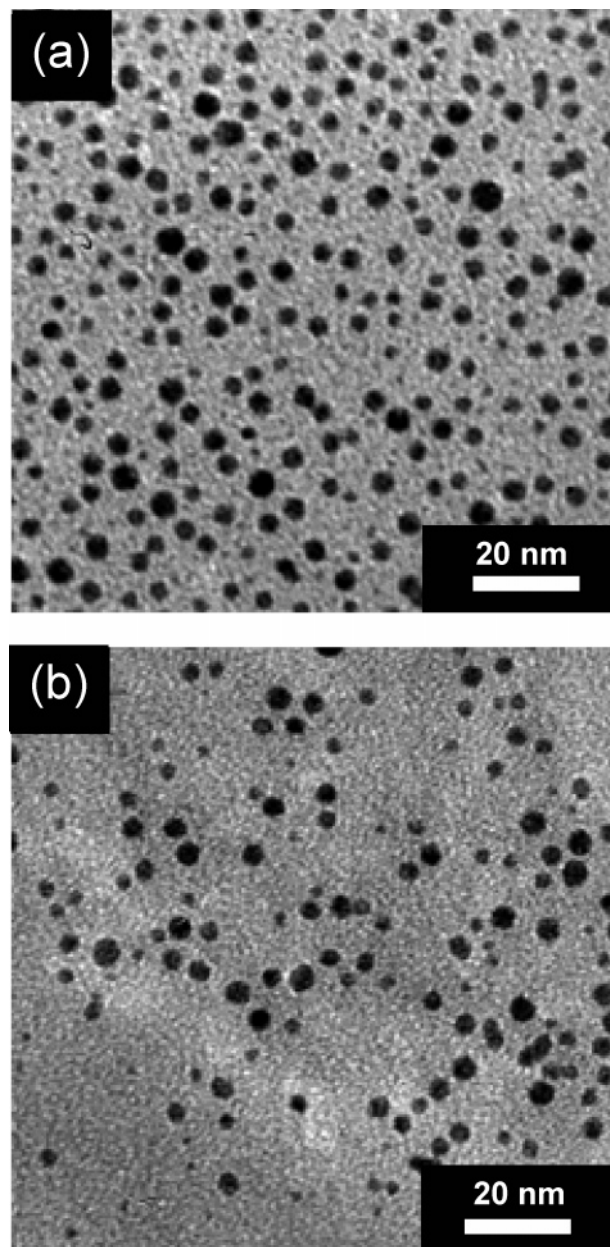


Figure 1. TEM image of colloidal AuPd alloy nanoparticles: (a) EG4 stabilized, $d = 4.2 \pm 1.0$ nm, and (b) tiopronin stabilized, $d = 4.2 \pm 1.2$ nm.

pump and probe, and A is a constant. When the thermal decay times are short compared to τ , eq 9 is equivalent to the Fourier transform of T_p . This infinite series cannot be reduced to a simple analytical form and we solve the system of equations, eqs 5–9, numerically.

3. Results

Figure 1 presents TEM images of AuPd-EG4 and AuPd-tiopronin nanoparticles dried from water. The diameter of the AuPd-EG4 nanoparticles is 4.2 ± 1.0 nm and the Pd atomic content is $\sim 8\%$ by XRF. The diameter of the AuPd-tiopronin nanoparticles is 4.2 ± 1.2 nm and the Pd atomic content is $\sim 10\%$ by XRF.

In Figure 2, we plot the transient change in optical absorption measured for thioalkylated ethylene glycol-stabilized AuPd alloy nanoparticles and tiopronin-stabilized AuPd nanoparticles. At very short delay times $t < 3$ ps, the transient absorption signal includes significant hot-electron effects, i.e., the electronic

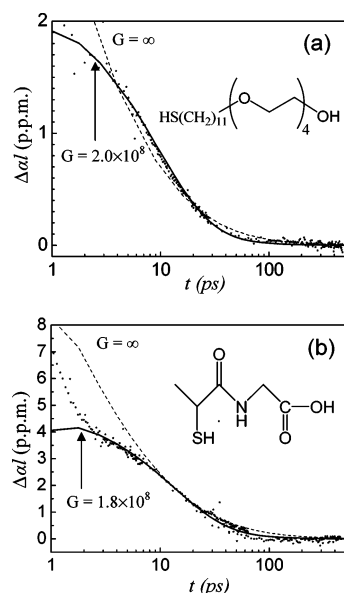


Figure 2. Transient changes in optical absorption from (a) suspensions of EG4-stabilized AuPd alloy nanoparticles in water (the pump power is 9 mW and the probe power is 10 mW; the sample path length $l = 0.2$ mm and the absorption length $\alpha^{-1} \approx 7$ mm) and (b) suspensions of tiopronin-stabilized AuPd nanoparticles in water (the pump power is 10 mW and the probe power is 15 mW, the sample path length $l = 0.2$ mm; and the absorption length $\alpha^{-1} \approx 8$ mm). The calculated thermal decays are obtained from eqs 5–9, assuming the particle diameter $d = 4.2$ nm. $G = \infty$ excludes interface effects (dashed line); $G = 200$ and $180 \text{ MW m}^{-2} \text{ K}^{-1}$ respectively are the lower limits on G that are consistent with the data in panels a and b (solid line). The chemical structures of EG4 and tiopronin are presented as insets.

excitations have not yet equilibrated with the lattice at $t < 3$ ps. These hot-electron signals appear to be negligible at $t > 3$ ps and we fit the data for $t > 3$ ps using eq 9 with two free parameters: the interface thermal conductance G and the value of the constant A that provides a scaling factor for the y-axis. All other parameters in the model are fixed; r is given by the TEM measurements, $C_p = 2.49 \text{ J cm}^{-3} \text{ K}^{-1}$, $C_f = 4.18 \text{ J cm}^{-3} \text{ K}^{-1}$, and $\Lambda_f = 0.60 \text{ W m}^{-1} \text{ K}^{-1}$. The best fit of the thermal model to the data gives $G \approx 250 \pm 90 \text{ MW m}^{-2} \text{ K}^{-1}$ for AuPd-EG4 and $145 \pm 55 \text{ MW m}^{-2} \text{ K}^{-1}$ for AuPd-tiopronin. The relatively large uncertainties in G are mostly the result of uncertainties in the measurements of the particle radius and uncertainties in the thermal model that result from the polydispersity of the particle radii.

Large-diameter particles ($d > 15$ nm) are difficult to synthesize with the one-phase alcoholic solution method; thus, we adopted the seed-growth method to synthesize Au-core AuPd-shell nanostructures in aqueous solution. The Au^{3+} and Pd^{2+} ions are reduced on the surface of 13-nm Au seed particles; this approach improves the control of the average particle radius and reduces the polydispersity.¹⁴ Because the composition of the AuPd shell is predominately Au, surface modifications using gold–thiol chemistry still operate. We vary the AuPd shell thicknesses by varying the density of Au seeds in the seed solution; these different mixtures are denoted AuPd-A through D. Au-F is a control sample in which there is no Pd^{2+} in the growth solution.

Figure 3 presents the UV–vis absorption spectra of the Au seeds, the core–shell nanoparticles, and the control sample Au-F. The plasmon absorption peak at 520 nm is mostly quenched in the Au-core/AuPd-shell nanoparticles, and as expected, the

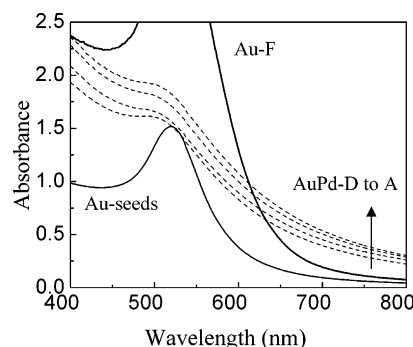


Figure 3. UV–vis absorption spectra of Au-seeds, AuPd-A through D with decreasing shell thickness, and control pure Au sample Au-F in water. The concentration of Au nanoparticles in the seed solution is $\sim 0.8 \text{ mg/10 mL}$; concentrations of the core–shell nanoparticles in samples AuPd-A through AuPd-D are ~ 1.1 to 1.3 mg/10 mL ; and for the pure Au control sample Au-F, the particle concentration is $\sim 1.6 \text{ mg/10 mL}$.

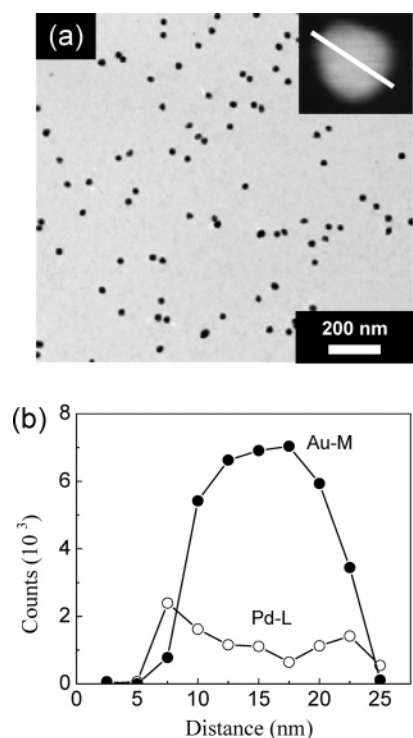


Figure 4. (a) TEM image of AuPd-D, diameter $d = 22 \pm 2$ nm; the inset is a higher magnification STEM image of one particle. (b) Au and Pd elemental distribution across this particle, using EDS line analysis.

absorption at 770 nm is larger than that of the control sample Au-F, even though Au-F has a large plasmon absorption peak at 520 nm.

The AuPd shell structure was confirmed through STEM and EDS analysis. Figure 4a is a TEM image of AuPd-D. The EDS line scan across the particles, Figure 4b, shows that the Au concentration peaks in the middle of the particle while the Pd peaks near the edges of the particle. The overall composition of AuPd-D nanoparticle is ~ 75 atom % Au and ~ 25 atom % Pd. Since the shell makes up 80% of the volume of the particle, the Pd content of the shell is only slightly larger than the average Pd content.

Figure 5 is the change of optical absorption of Au-core/AuPd-shell nanoparticles stabilized by a CTAB bilayer in water. The oscillations at short times are due to the breathing modes of the AuPd shell nanoparticles.²⁸ The period of these breathing

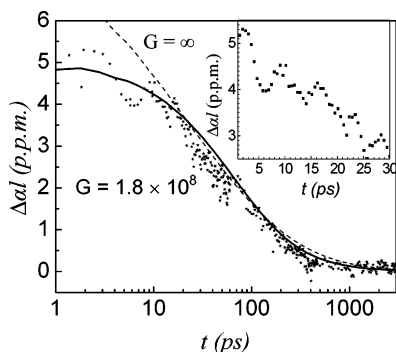


Figure 5. Transient changes in optical absorption from suspensions of CTAB-stabilized AuPd-D core/shell nanoparticles in water. The inset highlights the changes in the optical absorption produced by the breathing mode oscillations. The pump power is 13 mW and the probe power is 8 mW. The sample path length $l = 0.2$ mm and the absorption length $\alpha^{-1} \approx 6$ mm. The calculated thermal decays are obtained from eqs 5–9, using a particle diameter of $d = 22$ nm. $G = \infty$ excludes interface effects (dashed line); $G = 180 \text{ MW m}^{-2} \text{ K}^{-1}$ is the lower limit on G that is consistent with the data (solid line).

modes is predicted to be²⁹

$$\Gamma = \frac{D}{0.93v_l} \quad (10)$$

where v_l is the longitudinal speed of sound ($v_l = 3240$ m/s for Au) and D is the diameter of the particles. From the period $\Gamma = 6.8$ ps derived from the data plotted as the inset of Figure 5, the diameter of the particles is estimated to be 20 nm using $v_l(\text{Au}) = 3240$ m/s as an approximation for the core-shell nanoparticles, in good agreement with the diameter of 22 nm measured by TEM.

We fit the decay of the temperature of the particle as before with two free parameters; the best-fit through the middle of the breathing mode oscillations gives $G \approx 230 \pm 50 \text{ MW m}^{-2} \text{ K}^{-1}$. In this case, the uncertainties in the particle diameters is relatively small but the uncertainty in G is significant because the relatively large particle diameter makes the cooling rate less sensitive to the exact value of G .

Of the three AuPd nanoparticle systems studied, EG4-stabilized AuPd nanoparticles can also be dispersed in methanol and water/methanol mixtures. Figure 6a shows that in methanol, the decay is well-fit by the thermal model and G is large; unfortunately, the relatively small value of the thermal conductivity and heat capacities of alcohols in comparison to water makes the thermal decay less sensitive to G , see eq 3, and we can only set a lower limit, $G > 200 \text{ MW m}^{-2} \text{ K}^{-1}$.

In water/methanol mixtures, we consistently observe a long-time tail in the decay of the optical absorption, see Figure 6b. This behavior is highlighted in Figure 6c where we plot the

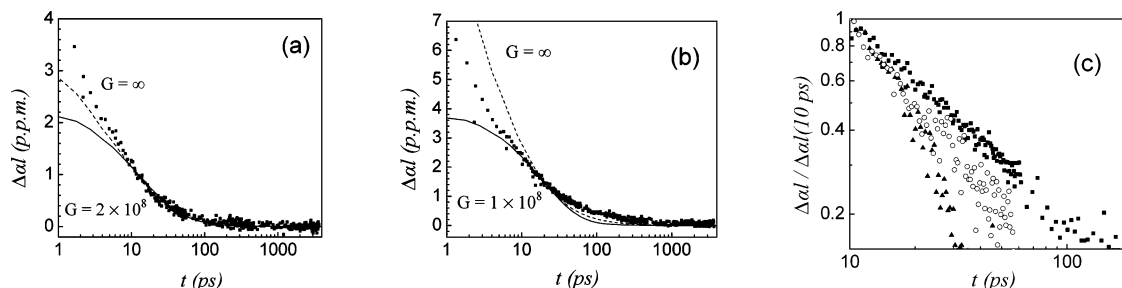


Figure 6. Transient changes in optical absorption from (a) EG4-stabilized AuPd in methanol (the pump power is 5 mW and the probe power is 8 mW), (b) EG4-stabilized AuPd in 50 vol % water/50 vol % methanol (the pump power is 9 mW and the probe power is 8 mW), and (c) normalized transient changes in optical absorption from suspensions of EG4-stabilized AuPd in pure water (solid triangles), pure methanol (open circles), and 50 vol % water/50 vol % methanol mixture (solid squares) (the sample path length $l = 0.2$ mm and the absorption length $\alpha^{-1} \approx 7$ mm).

normalized change of optical absorption of AuPd-EG4 dispersed in pure water, pure methanol, and water/methanol mixtures on a log-log scale. The most rapid thermal decay is in pure water and the thermal decay in methanol is only slightly slower. We do not yet understand the origins of the long-time tail of the thermal decay in methanol/water mixtures, but speculate that local ordering or reorganization of the solvent mixture near the particle surface may modify the optical properties of the suspension and contribute a slow component to the transient absorption signal.

4. Discussion and Conclusions

The thermal conductances of the interfaces between AuPd nanoparticles and water are remarkably insensitive to the chemistry and structure of the organic stabilizing group and are also insensitive to the particle diameter. We find $G \approx 250 \pm 90 \text{ MW m}^{-2} \text{ K}^{-1}$ for AuPd stabilized by thioalkylated ethylene glycol (EG4); $G \approx 145 \pm 55 \text{ MW m}^{-2} \text{ K}^{-1}$ for AuPd stabilized by tiopronin; and $G \approx 230 \pm 50 \text{ MW m}^{-2} \text{ K}^{-1}$ for Au-core/AuPd-shell particles stabilized by cetyltrimethylammonium bromide (CTAB). Therefore, we have confirmed and extended the generality of the high thermal conductance of nanoparticle-water interfaces that we previously observed for citrate-stabilized Pt nanoparticles.¹¹ The fact that the thermal conductance of the interface does not appear to be a function of capping chemistry in aqueous solution is unexpected.

We contrast these values for G in aqueous suspensions with data for the interface thermal conductance of alkanethiol-terminated Au and AuPd particles in an organic solvent, toluene. In ref 11 we reported a lower limit on G for pure Au nanoparticles, $G > 20 \text{ MW m}^{-2} \text{ K}^{-1}$, and for AuPd nanoparticles, we found $G \approx 5 \text{ MW m}^{-2} \text{ K}^{-1}$ although, admittedly, the fit of the data to the thermal model was particularly poor in the latter case. Because of this uncertainty, we prepared and measured new suspensions of alkanethiol-stabilized AuPd nanoparticles in toluene and have found $G \approx 15 \text{ MW m}^{-2} \text{ K}^{-1}$ (data not shown) with much better agreement between the data and the fit. Therefore, we conclude that G values for nanoparticle interfaces in typical aqueous suspensions are at least an order of magnitude larger than G values for nanoparticles in a typical organic solvent.

While we believe that these values for thermal conductance of solid-fluid interfaces are now experimentally well established, we can only speculate on the mechanisms that determine G in the various systems. In principle, the measured value of the interface conductance could include at least 4 processes: (i) the flow of heat from the nanoparticle into stabilizing the group; (ii) the flow of vibrational energy along the length of the stabilizing group or across the molecular layer; (iii) the transport of vibrational energy from the stabilizing group to the

surrounding fluid; and (iv) the possibility of the direct transfer of heat from the nanoparticle to fluid molecules that penetrate the self-assembled molecular layer of the organic stabilizing group.

The large difference in the values of G for toluene and water suspensions suggests that either the third or fourth mechanism listed above is playing a critical role since we do not have any reason to believe that the first two mechanisms would have a strong dependence on the solvent. The large values for the thermal conductance G of nanoparticles in aqueous solution may indicate that the thermal coupling between hydrophilic molecular layers and water is strong, while the thermal coupling between alkanethiol monolayers and toluene is much weaker, resulting in a smaller G . Strong thermal coupling also exists in suspensions of EG4-stabilized nanoparticles in methanol (Figure 6) and 2-propanol (data not shown). As of yet, we are not certain of the exact mechanism of the strong thermal coupling, but speculate that hydrogen bonding between the organic stabilizing group and the solvent may enhance the thermal coupling.

If we can assume that the thermal coupling between the particle and the organic stabilizing group and between the organic stabilizing group and water is strong, then G may be limited by heat transport within the self-assembled layer of the organic stabilizing group. In this case, we can envision the molecular layer as a thin polymer film with a thickness h ; the thermal conductance of the interface is then simply $G = \Lambda/h$. A typical value for the thermal conductivity of a polymer is $\Lambda \approx 0.20 \text{ W m}^{-1} \text{ K}^{-1}$; therefore, a layer of thickness 1 nm would produce a conductance of $G \approx 200 \text{ MW m}^{-2} \text{ K}^{-1}$, comparable to what we observe in aqueous suspensions.

Finally, we note that our experimental results of solid-liquid interface thermal conductance G may provide guidance on the design of selective targeting agents in laser-based medical therapies through control of the spatial extent of thermal damage³⁰ and optimization of the match between the time-scale of the thermal decays and the width of the laser pulses.

Acknowledgment. This work was supported by U.S. DOE Grant No. DEFG02-01ER45938. The Ti:sapphire laser is part of the Laser Facility of the Seitz Materials Research Laboratory at the University of Illinois. TEM characterization of the colloidal particles was carried out in the Center for Microanalysis of Materials, University of Illinois, which is partially supported by the U.S. Department of Energy under Grant No. DEFG02-96-ER45439. The authors thank Prof. J.-M. Zuo and W. Huang for the assistance with STEM and EDS and R. Shimmin for synthesizing EG4.

References and Notes

- (1) Cahill, D. G.; Goodson, K.; Majumdar, A. *J. Heat Transfer* **2002**, *124*, 223–241.
- (2) Cahill, D. G.; Ford, W. K.; Goodson, K. E.; Mahan, G. D.; Majumdar, A.; Maris, H. J.; Merlin, R.; Phillpot, S. R. *J. Appl. Phys.* **2003**, *93*, 793–818.
- (3) Costescu, R. M.; Cahill, D. G.; Fabreguette, F. H.; Sechrist, Z. A.; George, S. M. *Science* **2004**, *303*, 989–990.
- (4) Lee, S. M.; Cahill, D. G.; Venkatasubramanian, R. *Appl. Phys. Lett.* **1997**, *70*, 2957–2959.
- (5) Mahan, G. D.; Woods, L. M. *Phys. Rev. Lett.* **1998**, *80*, 4016–4019.
- (6) Torquato, S.; Hyun, S.; Donev, A. *Phys. Rev. Lett.* **2002**, *89*, 266601.
- (7) Eastman, J. A.; Choi, S. U. S.; Li, S.; Yu, W.; Thompson, L. J. *Appl. Phys. Lett.* **2001**, *78*, 718–720.
- (8) Huxtable, S. T.; Cahill, D. G.; Shenogin, S.; Xue, L. P.; Ozisik, R.; Barone, P.; Usrey, M.; Strano, M. S.; Siddons, G.; Shim, M.; Koblinski, P. *Nat. Mater.* **2003**, *2*, 731–734.
- (9) Hamad-Schifferli, K.; Schwartz, J. J.; Santos, A. T.; Zhang, S. G.; Jacobson, J. M. *Nature* **2002**, *415*, 152–155.
- (10) West, J. L.; Halas, N. J. *Annu. Rev. Biomed. Eng.* **2003**, *5*, 285–292.
- (11) Wilson, O. M.; Hu, X. Y.; Cahill, D. G.; Braun, P. V. *Phys. Rev. B* **2002**, *66*, 224301.
- (12) Templeton, A. C.; Chen, S. W.; Gross, S. M.; Murray, R. W. *Langmuir* **1999**, *15*, 66–76.
- (13) Kanaras, A. G.; Kamounah, F. S.; Schaumburg, K.; Kiely, C. J.; Brust, M. *Chem. Commun.* **2002**, 2294–2295.
- (14) Jana, N. R.; Gearheart, L.; Murphy, C. J. *Langmuir* **2001**, *17*, 6782–6786.
- (15) West, J. L.; Halas, N. J. *Curr. Opin. Biotechnol.* **2000**, *11*, 215–217.
- (16) Roberti, T. W.; Smith, B. A.; Zhang, J. Z. *J. Chem. Phys.* **1995**, *102*, 3860–3866.
- (17) Inouye, H.; Tanaka, K.; Tanahashi, I.; Hirao, K. *Phys. Rev. B* **1998**, *57*, 11334–11340.
- (18) Link, S.; Burda, C.; Wang, Z. L.; El-Sayed, M. A. *J. Chem. Phys.* **1999**, *111*, 1255–1264.
- (19) Halte, V.; Bigot, J. Y.; Palpant, B.; Broyer, M.; Prevel, B.; Perez, A. *Appl. Phys. Lett.* **1999**, *75*, 3799–3801.
- (20) Harata, A.; Taura, J.; Ogawa, T. *Jpn. J. Appl. Phys. I* **2000**, *39*, 2909–2912.
- (21) Hu, M.; Hartland, G. V. *J. Phys. Chem. B* **2002**, *106*, 7029–7033.
- (22) Hu, M.; Wang, X.; Hartland, G. V.; Salgueirino-Maceira, V.; Liz-Marzan, L. M. *Chem. Phys. Lett.* **2003**, *372*, 767–772.
- (23) Pale-Grosdemange, C.; Simon, E. S.; Prime, K. L.; Whitesides, G. M. *J. Am. Chem. Soc.* **1991**, *113*, 12–20.
- (24) Lu, L. H.; Wang, H. S.; Xi, S. Q.; Zhang, H. J. *J. Mater. Chem.* **2002**, *12*, 156–158.
- (25) Enustun, B. V.; Turkevich, J. *J. Am. Chem. Soc.* **1963**, *85*, 3317–3328.
- (26) Brust, M.; Walker, M.; Bethell, D.; Schiffrin, D. J.; Whyman, R. *J. Chem. Soc., Chem. Commun.* **1994**, 801–802.
- (27) O'Hara, K. E.; Hu, X. Y.; Cahill, D. G. *J. Appl. Phys.* **2001**, *90*, 4852–4858.
- (28) Hodak, J. H.; Henglein, A.; Hartland, G. V. *J. Chem. Phys.* **1999**, *111*, 8613–8621.
- (29) Tamura, A.; Higeta, K.; Ichinokawa, T. *J. Phys. C Solid State* **1982**, *15*, 4975–4991.
- (30) Gereon Huttman, R. B. *IEEE J. Sel. Top. Quantum Electron.* **1999**, *5*, 954–962.